Full Paper

Journal of the Brazilian Chemical Society

https://dx.doi.org/10.21577/0103-5053.20250076

J. Braz. Chem. Soc. **2025**, *36*, 9, e-20250076, 1-9

Highly Efficient Honeycomb Hypocrystalline V-P-C Catalysts for Sustainable Production of Acrylic Acid via Glycerol Dehydration-Oxidation

Xiaobing Zhao,[a] Weichen Wang,[a] Jun Liu,[,a] Meng Lian,[a] Youjun Yan,[a] Guofu Huang,[a] Yongwei Li[a] and Xinzhen Feng[b]*

[a]*Peninsula Engineering Research Center of Comprehensive Brine Utilization, Weifang University of Science and Technology, Weifang, 262700, China*

[b]*Key Laboratory of Mesoscopic Chemistry, MOE, School of Chemistry and Chemical Engineering, Nanjing University, Nanjing, 210023, China*

A series of hypocrystalline vanadium-phosphorus-carbon (V-P-C) catalysts, synthesized via a novel organic phosphoric acid-assisted strategy, were developed for the dehydration-oxidation of glycerol to acrylic acid. Among these, the VPO (vanadium-phosphorus oxide)-EDTPMA catalyst, derived from ethylenediamine tetramethylphosphonic acid (EDTPMA) as both phosphorus precursor and structure-directing agent, demonstrated exceptional performance, achieving 90% glycerol conversion with 53.4% selectivity to acrylic acid and 28.7% to acrolein under optimized conditions. Advanced characterization (X-ray diffraction (XRD), Raman, X-ray photoelectron spectroscopy (XPS), H_2 temperature-programmed reduction (H_2-TPR), scanning electron microscopy (SEM), and temperature-programmed desorption of ammonia (NH_3-TPD)) revealed that the thermal decomposition of amino groups in EDTPMA triggered a crystalline-to-hypocrystalline transition, generating a hybrid structure with preserved vanadium-phosphorus oxide phases embedded in an amorphous carbon matrix. This unique architecture introduced abundant oxygen vacancies and medium acid sites, which synergistically facilitated glycerol dehydration to acrolein and subsequent selective oxidation to acrylic acid. The hypocrystalline nature of VPO-EDTPMA enhanced redox cycling via vanadium species while mitigating over-oxidation pathways. This work provides a rational design strategy for multifunctional hypocrystalline catalysts, emphasizing the critical role of defect engineering in biomass valorization processes.

Keywords: glycerol, acrylic acid, hypocrystalline catalysts, vanadium-phosphorus oxide

Introduction

The extensive reliance on fossil fuels has historically underpinned global industrialization and economic growth,[1,2] yet their combustion has precipitated severe environmental crises through unabated CO_2 emissions.[3,4] In response, the Paris Agreement has galvanized efforts to transition toward renewable energy sources, with biodiesel emerging as a sustainable alternative.[5-7] However, biodiesel production via transesterification generates about 10 wt.% glycerol as a byproduct,[8-10] necessitating innovative strategies to valorize this surplus into high-value chemicals such as acrylic acid, a versatile precursor for polymers, detergents, and agrochemicals.[11-15] Current industrial acrylic acid production relies on petroleum-derived propylene, rendering glycerol-based routes economically and environmentally advantageous.[16]

As a typical acid-catalyzed reaction, glycerol can be converted into acrylic acid on catalysts that possess both Brønsted and Lewis acid sites. These catalysts encompass heteropolyacids,[17] zeolites,[18] metal oxides,[1,19-21] phosphates,[9] and sulfates.[22] For instance, phosphoric acid-modified HZSM-5 achieved 89.6% selectivity at full glycerol conversion,[5] while WO_3/ZrO_2@SiC enabled microwave-assisted reactions (250 °C) with > 70% selectivity.[1] MoP catalysts demonstrated 80% selectivity over 50 h,[14] and tungsten-based heteropolyacids revealed acid site density-dependent performance.[7] Despite these advances, such systems rely on crystalline frameworks, which inherently limit oxygen vacancy (O_V) concentrations and active site accessibility due to their rigid, defect-poor structures.[23]

Hypocrystalline materials, featuring a hybrid ordered-disordered atomic arrangement, present a paradigm shift

*e-mail: liujun@wfust.edu.cn
Editor handled this article: Juliano Alves Bonacin (Associate)

in catalysis. Their undercoordinated atoms and dangling bonds generate abundant O_Vs and electron-rich active sites,[24] while their flexible local structures enhance electron transfer efficiency.[25] Though hypocrystalline catalysts have shown promise in CO_2 hydrogenation,[24] oxygen evolution reaction,[25] and alkane oxidation,[26,27] their potential in glycerol valorization remains unexplored.

Herein, we design hypocrystalline vanadium-phosphorus-carbon (V-P-C) catalysts using organic phosphonic acid to unlock synergistic acid-redox functionalities for glycerol dehydration-oxidation. The hypocrystalline architecture, engineered via amino group decomposition in ethylenediamine tetramethylphosphonic acid (EDTPMA), preserves vanadium-phosphorus oxide phases while embedding them in an amorphous carbon matrix. This unique structure fosters numerous medium acid sites, oxygen vacancies, and redox-active V^{4+}/V^{5+} species, collectively enabling 90% glycerol conversion with 53.4% acrylic acid selectivity, outperforming conventional crystalline analogues. This work establishes hypocrystallinity as a critical lever for designing multifunctional catalysts in biomass upgrading.

Experimental

Materials and reagents

The involved chemical reagents, comprising vanadium pentoxide (V_2O_5) and four organophosphorus compounds, phenylphosphonic acid (PPOA, $C_6H_7O_3P$, 98%), *n*-hexylphosphonic acid (HPAA, $C_6H_{15}O_3P$, 99%), ethylenediamine tetramethylphosphonic acid (EDTPMA, $C_6H_{20}N_2O_{12}P_4$, 95%), along with glycerol, were procured at analytical reagent (AR) grade purity. All materials were used as received without further purification.

Catalyst preparation

Vanadium-phosphorus oxide (VPO) precursors were synthesized by mixing vanadium pentoxide (V_2O_5, 0.03 mol), stoichiometric organophosphonic acid (P/V molar ratio = 1), and deionized water (90 mL) in a stainless-steel autoclave. The suspension was hydrothermally treated at 140 °C with continuous stirring for 12 h. The resultant solid was collected via vacuum filtration, washed repeatedly with acetone to remove residual organics, and then dried under reduced pressure at 80 °C for 24 h. Three distinct precursors-designated as VPO-PPOA-Pre, VPO-HPAA-Pre, and VPO-EDTPMA-Pre, were obtained by employing phenylphosphonic acid (PPOA), *n*-hexylphosphonic acid (HPAA), and ethylenediamine tetramethylphosphonic acid (EDTPMA) as phosphorus sources, respectively.

The precursor powders were calcined in a tubular furnace under nitrogen atmosphere using the following protocol, heating from ambient temperature to 400 °C at a controlled ramp rate of 2° C min^{-1}, followed by isothermal retention for 16 h. This thermal treatment yielded the activated catalysts VPO-PPOA, VPO-HPAA, and VPO-EDTPMA, corresponding to their respective precursors.

Characterization of catalyst

The physical and chemical characteristics of the catalysts were investigated through a combination of advanced characterization techniques, including scanning electron microscopy (SEM), Raman, X-ray diffraction (XRD), X-ray photoelectron spectroscopy (XPS), H_2 temperature-programmed reduction (H_2-TPR), and temperature-programmed desorption of ammonia (NH_3-TPD).

XRD

Powder diffraction patterns were acquired on a Philips X'Pert MPD Pro diffractometer equipped with a graphite-monochromated Cu Kα radiation source (λ = 0.1541 nm). Scans were performed in the 2θ range of 10-80° at 0.02° step size.

Raman

Room-temperature spectra were collected on a HORIBA LabRAM HR Evolution spectrometer with a 532 nm diode laser excitation source.

XPS

The binding energy (BE) was calibrated against the C1s signal (284.6 eV) of contaminant carbon. Elemental surface composition was estimated on the basis of peak areas normalized using Wagner factors. Relative surface concentration of C, V, and O element with different states can be estimated through deconvolution analysis of the corresponding XPS peak. For the same batch of sample measured under identical conditions as well as the same parameters adopted for deconvolution analysis.

H_2-TPR

Reduction behavior was analyzed in a quartz microreactor loaded with 100 mg catalyst. Samples were pretreated in Ar (40 mL min^{-1}) at 200 °C for 1 h, then cooled to 25 °C. Temperature-programmed reduction was conducted under 5% H_2/Ar (40 mL min^{-1}) from 25 to 850 °C at 10 °C min^{-1}, followed by isothermal holding

until baseline stabilization. Hydrogen consumption was monitored by thermal conductivity detection (TCD).

NH_3-TPD

Catalyst of 50 mg was first heated in an Ar flow (40 mL min^{-1}) to 200 °C and kept at this temperature for 1 h. Then, the sample was cooled to 50 °C in the Ar flow. After that, NH_3 adsorption was performed at 50 °C for 1 h. Finally, NH_3-TPD was carried out in an Ar flow (40 mL min^{-1}) with the sample being heated to 500 °C at a rate of 10 °C min^{-1}. The amount of desorbed NH_3 (in μmol g^{-1}) was determined by a titration, in which a HCl solution (0.01 mol L^{-1}) was used to absorb the released NH_3. A NaOH solution (0.01 mol L^{-1}) was used as the titrant.

Catalyst evaluation

Catalytic performance assessment was conducted through a fixed-bed reactor system for the gas-phase dehydration-oxidation of glycerol to acrylic acid under atmospheric pressure. Prior to testing, catalyst precursors were pelletized, mechanically crushed, and sieved to obtain 20-40 mesh granules. A straight quartz tubular reactor (internal diameter (ID) = 10 mm) was loaded with 0.5 g of catalyst bed, followed by quartz sand of the same mesh size to fill the remaining space. The catalyst activation protocol comprised three sequential steps, (*i*) thermal pretreatment under continuous N_2 flow (30 mL min^{-1}) with temperature programming from ambient to 320 °C at 10 °C min^{-1} ramp rate, (*ii*) isothermal conditioning at 320 °C for 2.5 h, followed by (*iii*) system equilibration to reaction temperature. The reaction was initiated by introducing an aqueous glycerol feed (27.36 mmol glycerol h^{-1}) through a calibrated micro-syringe pump, with air serving as both oxidant and carrier gas (total flow rate optimized through preliminary experiments). Liquid products were continuously collected using a dual-stage cold trap system maintained at 5 °C to prevent volatile loss, while gaseous effluents were periodically sampled through a six-port valve for online analysis via thermal conductivity detector (TCD). Post-reaction liquid mixtures were quantitatively analyzed using gas chromatography (GC-126N system equipped with flame ionization detector) employing an HP-FFAP capillary column (25 m × 0.32 mm × 0.5 μm). Identification and quantification of acrylic acid, acrolein, and other oxygenates were achieved through external calibration with certified reference standards.

The conversion of glycerol (X_{Gly}), the selectivity of products (S_x) and carbon balance (CB) were calculated as follows:

$$X_{Gly}(\%) = \frac{n^0_{Gly} - n_{Gly}}{n^0_{Gly}} \times 100 \quad (1)$$

$$S_x(\%) = \frac{n_x}{n^0_{EO} - n_{Gly}} \times 100 \quad (2)$$

$$FR_{Acr} = \frac{n_{AA}}{m_{Cat} \times t} \quad (3)$$

$$CB(\%) = \frac{N_{Gly} \times n_{Gly} + N_{Acr} \times n_{Acr} + N_{AA} \times n_{AA} + N_{HAc} \times n_{HAc} + N_{MeCHO} \times n_{MeCHO} + N_{CO} \times n_{CO} + N_{CO_2} \times n_{CO_2}}{N_{Gly} \times n^0_{Gly}} \times 100 \quad (4)$$

where, n_{Gly} is the molar quantity of unreacted glycerol (mmol), n^0_{Gly} is the molar quantity of glycerol fed into the reactor (mmol), n_x is the molar quantity of glycerol equivalent to products such as acrolein (Acr), acrylic acid (AA), acetic acid (HAc), acetaldehyde (MeCHO), and CO_x, N is the number of carbons in a specific molecule, n is the mole quantity of each component measured by gas chromatography (GC).

Results and Discussion

Morphology analysis

Figure 1 presents comparative SEM analyses of catalyst precursors synthesized with different phosphorus sources. Upon the activation process, a significant alteration of the catalyst morphology is observed, particularly evident in the fusion of the layers for VPO-HPAA and the absence of lamellar morphology for VPO-PPOA. Notably, the catalyst VPO-EDTPMA exhibits a distinct porous honeycomb structure due to the decomposition of amidogen during roasting, which provides abundant active sites and facilitates favorable mass transfer conditions for catalytic reactions.

Structure and phase composition analysis

Figure 2 presents the XRD patterns of catalyst precursors (designated as VPO-PPOA-Pre, VPO-HPAA-Pre, and VPO-EDTPMA-Pre) and their activated counterparts. All precursors exhibit distinct crystalline phases corresponding to phenylphosphonate,[28] *n*-hexylphosphonate,[29] and ethylenediamine tetramethylphosphonate,[30] respectively. Thermal activation induces notable crystallinity degradation, attributable to hydrogen-bond network collapse during organic component pyrolysis, ultimately yielding hypocrystalline architectures. Furthermore, distinct phase compositions are observed for catalysts obtained from different precursors, (*i*) VPO-PPOA exclusively displays $VOPO_4 \cdot 2H_2O$ (PDF No. 36-1472), (*ii*) VPO-HPAA

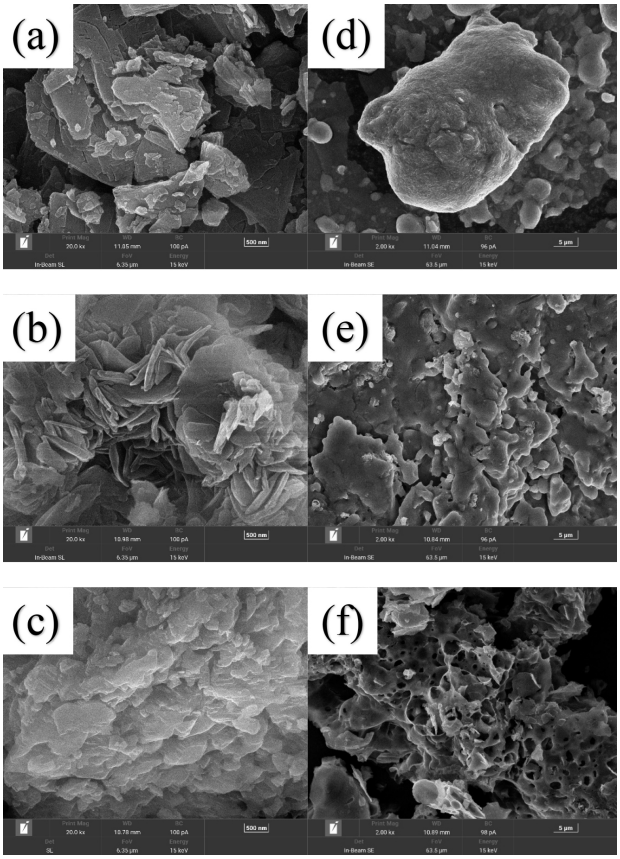

Figure 1. SEM images of the catalysts, (a) VPO-PPOA-Pre, (b) VPO-HPAA-Pre, (c) VPO-EDTPMA-Pre, (d) VPO-PPOA, (e) VPO-HPAA, and (f) VPO-EDTPMA.

shows coexisting $VOPO_4{\cdot}2H_2O$ (PDF No. 36-1472) and δ-$VOPO_4$ (PDF No. 47-0951), while (*iii*) VPO-EDTPMA uniquely converts to $VOHPO_3{\cdot}3H_2O$ (PDF No. 45-0578). This phase evolution confirms $V^{5+}\rightarrow V^{4+}$ reduction in VPO-EDTPMA through organic nitrogen elimination during activation.

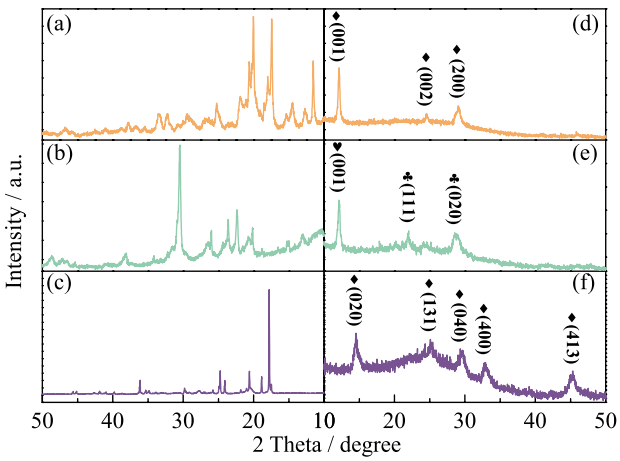

Figure 2. XRD patterns of the catalysts, (a) VPO-PPOA-Pre, (b) VPO-HPAA-Pre, (c) VPO-EDTPMA-Pre, (d) VPO-PPOA, (e) VPO-HPAA, and (f) VPO-EDTPMA. ♣-δ-$VOPO_4$ PDF No. 47-0951, ♦-$VOHPO_3{\cdot}3H_2O$ PDF No. 45-0578, ♥-$VOPO_4{\cdot}2H_2O$ PDF No. 36-1472.

Complementary Raman spectroscopy overcomes XRD limitations in characterizing hypocrystalline systems.[31,32] The vibrations associated with P–O and V–O typically manifest in the range of 850-1200 cm^{-1}.[33] The vibrations associated with amorphous carbon, on the other hand, can be observed within the range of 850 to 2000 cm^{-1}.[26] As shown in Figure 3, the peaks observed at 991 cm^{-1} can be attributed to the vibrations of V–O,[34] while those at 961, 919, and 885 cm^{-1} correspond to the vibrations of P–O under different chemical environments.[34-36] These variations arise from the influence of various alkyl groups of organic phosphinic acids. The activated catalysts also demonstrate distinct phase compositions. For instance, the catalyst VPO-PPOA comprises δ-$VOPO_4$, $VOPO_4{\cdot}2H_2O$, and $(VO)_2P_2O_7$ phases. The catalyst VPO-HPAA contains δ-$VOPO_4$ and $(VO)_2P_2O_7$ phases. The catalyst VPO-EDTPMA is composed exclusively of $VOPO_3{\cdot}3H_2O$ phases. Notably, the characteristic peaks associated with disordered carbon (1350 cm^{-1}, D band) and graphite sp^2 carbon (1560 cm^{-1}, G band) are also revealed in VPO-EDTPMA. It suggests a significant presence of amorphous carbon in catalyst VPO-EDTPMA. As literature reports,[23] amorphous carbon possesses abundant active sites, oxygen vacancies, high oxygen mobility, and large surface area due to unsaturated coordination and numerous defects on the surface atoms. In contrast, the relatively perfect crystal surface structure of crystalline catalysts restricts both the type and quantity of surface oxygen.

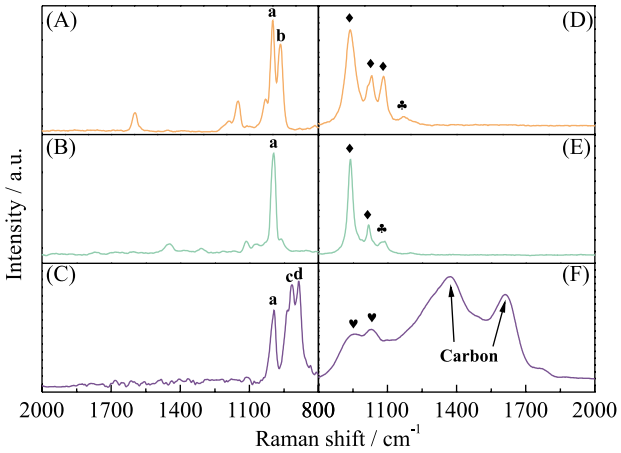

Figure 3. Raman spectra of the catalysts, (A) VPO-PPOA-Pre, (B) VPO-HPAA-Pre, (C) VPO-EDTPMA-Pre, (D) VPO-PPOA, (E) VPO-HPAA, and (F) VPO-EDTPMA. ♣-δ-$VOPO_4$, ♥-$VOHPO_3{\cdot}3H_2O$, ♦-$(VO)_2P_2O_7$, (a) V–O, (b) P–O, (c) P–O, (d) P–O.

Surface composition and state analysis

The H_2-TPR profiles of all catalysts exhibit two distinct reduction peaks upon deconvolution (Figure 4). The lower-temperature peaks (< 700 °C) are attributed

to the reduction of V^{5+} species, whereas the high-temperature region (> 700 °C) corresponds to V^{4+} reduction.[37] Hydrogen consumption was quantified using CuO as calibration reference. As summarized in Table S1 (Supplementary Information (SI) section), VPO-EDTPMA demonstrates significantly enhanced V^{4+} surface concentration (V^{4+}/V^{5+} = 2.16) compared to VPO-PPOA (V^{4+}/V^{5+} = 0.29) and VPO-HPAA (V^{4+}/V^{5+} = 0.31), accompanied by a notable 30 °C reduction in V^{5+} reduction temperature. This phenomenon suggests that the thermal elimination of organic nitrogen during precursor activation induces structural defects and unsaturated bonds in the hypocrystalline framework, thereby generating abundant reactive oxygen sites.

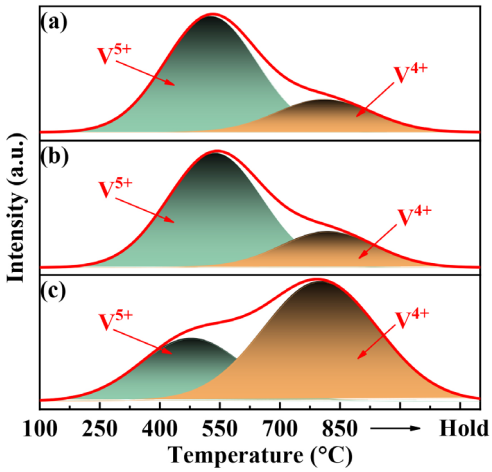

Figure 4. H_2-TPR profiles of the catalysts: (a) VPO-PPOA, (b) VPO-HPAA, and (c) VPO-EDTPMA.

Complementary XPS analysis reveals significant variations in surface composition influenced by phosphorus precursors. As revealed by the data in Table S2 (SI section), the catalysts exhibit substantial C content in addition to the characteristic V, P, and O elements, primarily attributed to the carbonization of organic alkyl phosphate during the thermal activation process. Notably, the absence of N element in catalyst VPO-EDTPMA confirms the thorough decomposition of amino-containing groups under the applied activation conditions. Deconvolution of the V 2p spectra (Figure 5) confirms the coexistence of V^{5+} and V^{4+} species.[38,39] Notably, VPO-EDTPMA exhibits the highest V^{4+} concentration among the catalysts (Table S3, SI section), corroborating the H_2-TPR findings. This consistency strongly supports the hypothesis that amino-containing precursors facilitate V^{5+} reduction.

The oxygen speciation analysis (Figure 6) resolves the O 1s spectrum into two components, lattice oxygen (O_L) and oxygen vacancies (O_V).[40,41] Quantitative analysis (Table S4, SI section) shows VPO-EDTPMA possesses the highest O_V

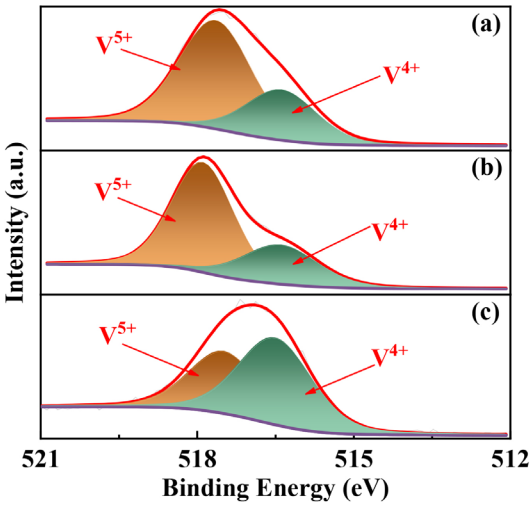

Figure 5. XPS spectra of V $2p_{3/2}$ for the catalysts: (a) VPO-PPOA, (b) VPO-HPAA, and (c) VPO-EDTPMA.

concentration, greater than other catalysts. This structural evolution from crystalline to defect-rich hypocrystalline phase during amine removal creates electron-deficient layers,[40] thereby driving redox reactions. It suggests that the activation process results in the removal of amino groups, leading to a transformation from crystalline to hypocrystalline structure and subsequently promoting O_V formation. The presence of O_V has been documented to increase the number of surface hydroxyl groups, thereby enhancing the density of Lewis acid sites on the catalyst surface and improving the catalytic performance.[42] It also elucidates why catalyst VPO-EDTPMA with the highest number of O_V exhibits more potent catalytic activity.

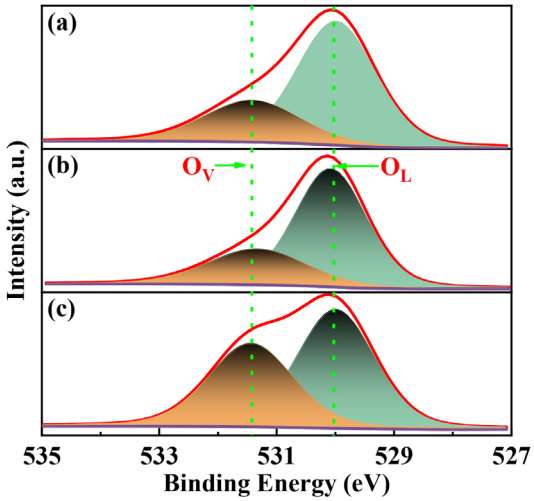

Figure 6. XPS spectra of O 1s for the catalysts: (a) VPO-PPOA, (b) VPO-HPAA, and (c) VPO-EDTPMA.

Surface acidity and catalytic performance

The target reaction represents a prototypical acid-

catalyzed dehydration-oxidation process, necessitating comprehensive evaluation of catalyst surface acidity through NH_3-TPD to establish structure-activity correlations. As shown in Figure 7, the NH_3 desorption profile displays three characteristic peaks corresponding to weak (140-170 °C), medium (320-350 °C), and strong acid sites (400-430 °C).[43] Quantitative analysis (Table S5, SI section) reveals that the VPO-EDTPMA catalyst, while demonstrating the lowest total acidity and complete absence of strong acid sites, exhibits exceptional medium acid site density. This distinctive acid distribution originates from its unique composition containing multiple vanadium oxidation states and abundant oxygen vacancies (O_V), as corroborated by XPS and H_2-TPR results. Notably, prior studies[31] have established a direct correlation between medium acid site concentration and target product selectivity in acid-catalyzed acrylic acid synthesis, providing a mechanistic rationale for the superior catalytic performance of VPO-EDTPMA.

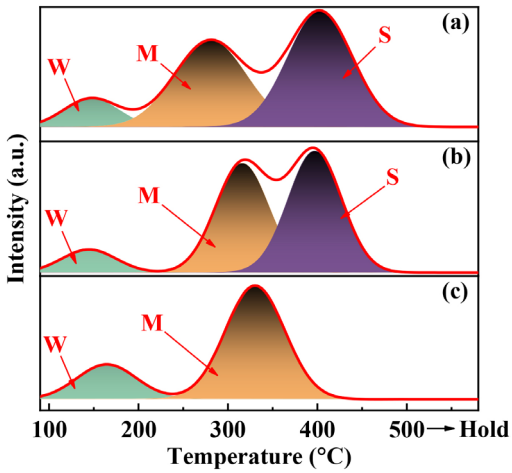

Figure 7. NH_3-TPD profiles of the catalysts: (a) VPO-PPOA, (b) VPO-HPAA, and (c) VPO-EDTPMA. W: weak; M: medium; S: strong.

Catalytic evaluation under ambient pressure glycerol conversion conditions (Figure 8 and Table S6, SI section) demonstrates marked performance differences between precursor and activated catalysts. While precursor materials showed negligible glycerol conversion and poor acrylic acid selectivity, activated catalysts achieved > 90% glycerol conversion with exceptional product selectivity, particularly with catalyst VPO-EDTPMA, which exhibits an impressive selectivity of 53.4% for acrylic acid and 28.7% for acrolein. The superior performance can be ascribed to its hypocrystalline structure and abundant medium acid sites on the surface. The catalyst VPO-EDTPMA is also notable for its excellent carbon balance, which is attributed to the higher content of V^{4+} species. This feature effectively prevents excessive oxidation of the target products and results in significantly lower CO_x selectivity.

Multitechnique characterization (Raman, XPS, H_2-TPR, SEM, NH_3-TPD) reveals a coherent structure-function relationship. During the catalyst preparation process, the presence of amino groups in EDTPMA induces a transition of the catalyst from crystalline to hypocrystalline while preserving the fundamental vanadium-phosphorus oxide phases. The transformation generates numerous amorphous components within the hypocrystalline structure, resulting in a proliferation of O_V and active sites on the catalyst surface. Moreover, it facilitates the formation of a significant number of medium acid sites that promote the target reaction. Additionally, this conversion leads to the development of a porous honeycomb architecture which enhances catalytic activity.

Previous studies[44] have systematically elucidated the catalytic mechanism of glycerol dehydration and oxidation over solid acid catalysts. Initially, glycerol is adsorbed onto the catalytic active site via its C_α–OH group, initiating the reaction. Subsequently, the synergistic transfer of C_α–H and the cleavage of the C_α–O bond facilitate the formation of ketene intermediates. These transient species are then converted into thermodynamically stable enols through tautomerization reactions. Finally, the C–O bond is broken with the concurrent elimination of water molecules, completing the formation of acrolein and its further oxidation to acrylic acid. Kinetic analysis reveals that the initial chemisorption process and the formation of ketene intermediates are the rate-determining steps. Oxygen vacancies (O_V) have been demonstrated to play a pivotal role in modulating catalytic performance via two primary mechanisms. Firstly, these defects markedly enhance the density of acidic sites on the surface by introducing unsaturated metal centers, thereby significantly improving the adsorption capacity of oxygen-containing substrates.[45] Secondly, O_V induce a redistribution of the electronic structure on the catalyst surface, particularly altering the energy states of the p-orbitals of adjacent oxygen atoms.[46] This electronic effect enhances the nucleophilic properties of the active sites, effectively promoting α-H abstraction and stabilizing the ketene intermediates during the rate-limiting step. In this study, the hypocrystalline catalyst VPO-EDTPMA rich in surface oxygen vacancies exhibited a substantial increase in the density of medium-strength acidic sites, which greatly facilitated the initial chemisorption process and the formation of ketene intermediates, ultimately demonstrating superior catalytic performance.

Under analogous reaction conditions, the catalytic performance of hypocrystalline catalyst VPO-EDTPMA and crystalline catalysts (Mo-V, V/H-b, and $Mo_xV_yO_z$) was systematically evaluated for the dehydration oxidation of glycerol (Table S7, SI section). Crystalline catalysts

demonstrate high glycerol conversion and acrylic acid selectivity due to their well-defined active site geometry and thermodynamic stability. However, the formation rate of acrylic acid on crystalline catalysts is significantly lower compared to that on the hypocrystalline catalyst VPO-EDTPMA. This discrepancy can be ascribed to the limited density of accessible active sites on the crystalline surface, which is constrained by the rigid lattice structure, thereby impeding the realization of high-throughput reaction kinetics. In contrast, the hypocrystalline catalyst VPO-EDTPMA exhibits a porous honeycomb structure, offering a higher density of active sites. Consequently, this structure renders the hypocrystalline catalyst VPO-EDTPMA more conducive to high-throughput reactions.

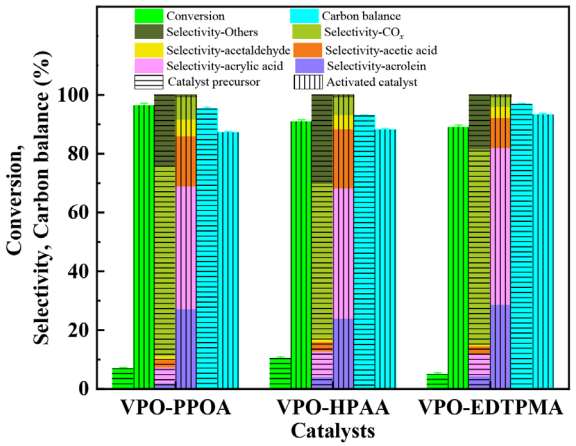

Figure 8. Catalytic activity of the catalysts, the reaction temperature and carrier flow rate were 320 °C and 30 mL min^{-1} (air), respectively. The liquid feed was a glycerol aqueous solution (10 wt.%), with a LHSV of 3 mL h^{-1}.

In this study, the mass transfer limitation of the reaction system was quantitatively assessed through systematic parameter analysis. As depicted in Figure 9, within the extensive control range of key parameters (reactant feed rate of 3-9 mL h^{-1}, carrier flow rate of 30-90 mL h^{-1}, and catalyst amount of 0.5-1.5 g), the catalytic efficiency remained consistently within a little fluctuation, demonstrating exceptional operational stability. Notably, variations in catalyst particle size within the 40-60 mesh range did not result in any discernible performance degradation. This observation indicates that the reaction kinetics are predominantly governed by the intrinsic chemical reaction rate rather than the external mass transfer process. A deeper investigation reveals that the distinctive hierarchical pore structure of the hypocrystalline catalyst VPO-EDTPMA, which comprises interconnected honeycomb pores and mesoporous channels, forms a three-dimensional diffusion network. This network ensures the rapid transport of reactant molecules within the catalyst phase, thereby significantly reducing sensitivity to mass transfer conditions.

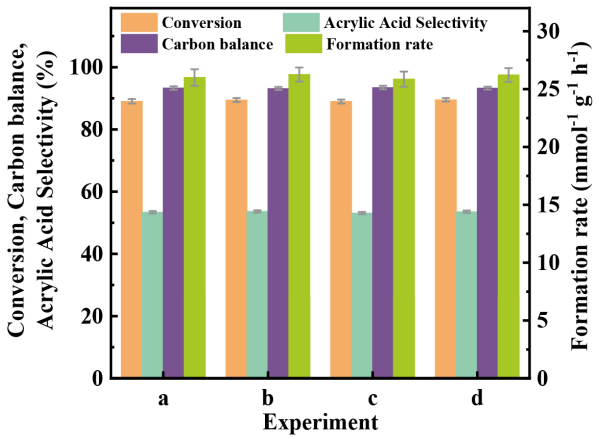

Figure 9. Catalytic performance of the catalyst VPO-EDTPMA, (a) carrier flow rate = 30 mL min^{-1}, liquid feed rate (LHSV) = 3 mL h^{-1}, catalyst amount = 0.5 g (20-40 mesh); (b) carrier flow rate = 60 mL min^{-1}, LHSV = 6 mL h^{-1}, catalyst amount = 1.0 g (20-40 mesh); (c) carrier flow rate = 90 mL min^{-1}, LHSV = 9 mL h^{-1}, catalyst amount = 1.5 g (20-40 mesh); (d) carrier flow rate = 30 mL min^{-1}, LHSV = 3 mL h^{-1}, catalyst amount = 0.5 g (40-60 mesh).

Conclusions

In this study, a series of hypocrystalline vanadium phosphorus oxide (VPO) catalysts were synthesized through an organic phosphoric acid-assisted route, with subsequent evaluation of their catalytic performance in glycerol dehydration-oxidation for acrylic acid production. Notably, the VPO-EDTPMA catalyst, prepared using EDTPMA as the phosphorus precursor, demonstrates enhanced hypocrystalline structural features and superior catalytic activity compared to its crystalline VPO counterpart. Comprehensive characterization through XRD, Raman, SEM, H_2-TPR, XPS, and NH_3-TPD reveals that the choice of organic phosphoric acid critically modulates both acid site distribution and catalytic functionality. The unique hypocrystalline architecture facilitates the generation of abundant oxygen vacancies (O_V) and mixed-valence vanadium species (V^{4+}/V^{5+}), which synergistically create a high density of medium-strength acid sites. These optimized acid sites exhibit remarkable specificity for the dehydration-oxidation reaction. Furthermore, the crystalline-to-hypocrystalline phase transition promotes the porous honeycomb structures, effectively increasing accessible active surfaces and mass transfer efficiency, ultimately resulting in enhancement in acrylic acid yield relative to conventional crystalline catalysts.

Supplementary Information

Supplementary information is available free of charge at http://jbcs.sbq.org.br as PDF file.

Acknowledgments

The financial support of Key R&D Program of Shandong Province (2024TSGC0990), Weifang University of Science and Technology Fund (KJRC2020007, 2024XJKJ02), and Project of Weifang Science and Technology Development Plan (2024JZ0009) were greatly appreciated.

Author Contributions

Jun Liu, Xiaobing Zhao, and Xinzhen Feng designed and conducted this research. Xiaobing Zhao, Weichen Wang, and Youjun Yan analyzed data. Jun Liu, Xiaobing Zhao, and Xinzhen Feng wrote the paper. Jun Liu, Guofu Huang, Yongwei Li, and Meng Liang plotted the figures. Jun Liu and Xinzhen Feng edited the whole manuscript.

References

1. Xie, Q.; Li, S.; Gong, R.; Zheng, G.; Wang, Y.; Xu, P.; Duan, Y.; Yu, S.; Lu, M.; Ji, W.; Nie, Y.; Ji, J.; *Appl. Catal., B* **2019**, *243*, 455. [Crossref]
2. Wu, S.; She, Q.; Tesser, R.; Di Serio, M.; Zhou, C.; *Catal. Rev.: Sci. Eng.* **2020**, *43*, 481. [Crossref]
3. Zengin, Y.; Kaya, B.; Boroglu, M.; Boz, I.; *Ind. Eng. Chem. Res.* **2023**, *62*, 1852. [Crossref]
4. Li, C.; Li, D.; Yin, S.; Wang, Z.; Liu, C.; Zhou, C.; *Appl. Catal., A* **2023**, *665*, 119355. [Crossref]
5. Shan, J.; Li, Z.; Chen, Z.; Wang, D.; Zhang, X.; Ning, Z.; Xue, Y.; Zhu, S.; *Chem. Eng. J.* **2023**, *460*, 141741. [Crossref]
6. Cui, M.; Mi, M.; Zhang, Y.; Xu, W.; Wang, M.; Shao, R.; Ding, J.; *New J. Chem.* **2023**, *47*, 1342. [Crossref]
7. Wang, Z.; Liu, L.; *Catal. Today* **2021**, *376*, 55. [Crossref]
8. Zhao, S.; Wang, W.; Wang, L.; Wang, W.; Huang, J.; *J. Catal.* **2020**, *389*, 166. [Crossref]
9. Ren, X.; Zhang, F.; Sudhakar, M.; Wang, N.; Dai, J.; Liu, L.; *Catal. Today* **2019**, *332*, 20. [Crossref]
10. Ginjupalli, S.; Balla, P.; Shaik, H.; Nekkala, N.; Ponnala, B.; Mitta, H.; *New J. Chem.* **2019**, *43*, 16860. [Crossref]
11. Feng, Y.; Yin, H.; Wang, A.; Shen, L.; Yu, L.; Jiang, T.; *Chem. Eng. J.* **2011**, *168*, 403. [Crossref]
12. Gong, L.; Lu, Y.; Ding, Y.; Lin, R.; Li, J.; Dong, W.; Wang, T.; Chen, W.; *Appl. Catal., A* **2010**, *390*, 119. [Crossref]
13. Sun, D.; Yamada, Y.; Sato, S.; Ueda, W.; *Green Chem.* **2017**, *19*, 3186. [Crossref]
14. Liu, S.; Yu, Z.; Wang, Y.; Sun, Z.; Liu, Y.; Shi, C.; Wang, A.; *Catal. Today* **2021**, *379*, 132. [Crossref]
15. Zhang, J.; Zhao, J.; Cui, X.; Hou, X.; Su, L.; Wang, H.; Deng, T.; *New J. Chem.* **2020**, *44*, 21332. [Crossref]
16. Ali, B.; Lan, X.; Arslan, M.; Wang, H.; Gilani, S.; Wang, S.; Wang, T.; *ACS Appl. Nano Mater.* **2020**, *3*, 10966. [Crossref]
17. Ma, T.; Ding, J.; Shao, R.; Xu, W.; Yun, Z.; *Chem. Eng. J.* **2017**, *316*, 797. [Crossref]
18. Carriço, C.; Cruz, F.; dos Santos, M.; Oliveira, D.; Pastore, H.; Andrade, H.; Mascarenhas, A.; *J. Catal.* **2016**, *334*, 34. [Crossref]
19. Cecilia, J. A.; García-Sancho, C.; Mérida-Robles, J. M.; Santamaría González, J.; Moreno-Tost, R.; Maireles-Torres, P.; *Appl. Catal., A* **2016**, *516*, 30. [Crossref]
20. García-Sancho, C.; Cecilia, J. A.; Moreno-Ruiz, A.; Mérida-Robles, J. M.; Santamaría-González, J.; Moreno-Tost, R.; Maireles-Torres, P.; *Appl. Catal., B* **2015**, *179*, 139. [Crossref]
21. Mahdavi, V.; Monajemi, A.; *RSC Adv.* **2016**, *6*, 114244. [Crossref]
22. Cavani, F.; Guidetti, S.; Marinelli, L.; Piccinini, M.; Ghedini, E.; Signoretto, M.; *Appl. Catal., B* **2010**, *100*, 197. [Crossref]
23. Yu, Y.; Liu, S.; Ji, J.; Huang, H.; *Catal. Sci. Technol.* **2019**, *9*, 5090. [Crossref]
24. He, J.; Chang, S.; Du, H.; Jiang, B.; Yu, W.; Wang, Z.; Chu, W.; Han, L.; Zhu, J.; Li, H.; *J. CO_2 Util.* **2021**, *54*, 101751. [Crossref]
25. Wei, Q.; Tan, X.; Zhang, J.; Yang, L.; Cao, L.; Dong, B.; *J. Colloid Interf. Sci.* **2021**, *586*, 505. [Crossref]
26. Xiao, C.; Du, Z.; Li, S.; Zhao, Y.; Liang, C.; *ChemCatChem* **2020**, *12*, 3650. [Crossref]
27. Hutchings, G.; Lopez-Sanchez, J.; Bartley, J.; Webster, J.; Burrows, A.; Kiely, C.; Carley, A.; Rhodes, C.; Hävecker, M.; Knop-Gericke, A.; Mayer, R.; Schlögl, R.; Volta, J.; Poliakoff, M.; *J. Catal.* **2002**, *208*, 197. [Crossref]
28. Wilke, M.; Buzanich, A. G.; Reinholz, U.; Rademann, K.; Emmerling, F.; *Dalton Trans.* **2016**, *45*, 9460. [Crossref]
29. Hu, Y.; Zhang, Y.; Li, C.; Wang, L.; Du, Y.; Mo, G.; Li, X.; Cheetham, A.; Wang, J.; *Adv. Mater.* **2019**, *31*, 1901124. [Crossref]
30. Larionov, D. S.; Bitanova, V. A.; Evdokimov, P. V.; Garshev, A. V.; Putlyaev, V. I.; *Inorg. Mater.* **2022**, *58*, 302. [Crossref]
31. Liu, J.; Wang, P.; Feng, Y.; Xu, Z.; Feng, X.; Ji, W.; Au, C.; *J. Catal.* **2019**, *374*, 171. [Crossref]
32. Preston, C. M.; Adams, W. A.; *J. Phys. Chem.* **1979**, *83*, 814. [Crossref]
33. Feng, X.; Sun, B.; Yao, Y.; Su, Q.; Ji, W.; Au, C.; *J. Catal.* **2014**, *314*, 132. [Crossref]
34. Oliveira, E. M.; Rogero, M.; Ferreira, E. C.; Gomes Neto, J. A.; *Spectrochim. Acta, Part A* **2021**, *246*, 119025. [Crossref]
35. Umeda, J.; Moriya, M.; Sakamoto, W.; Yogo, T.; *J. Membrane Sci.* **2009**, *326*, 701. [Crossref]
36. Cukrowski, I.; Popović, L.; Barnard, W.; Paul, S.; van Rooyen, P.; Liles, D.; *Bone* **2007**, *41*, 668. [Crossref]
37. Liu, J.; Wang, P.; Xu, P.; Xu, Z.; Feng, X.; Ji, W.; Arandiyan, H.; Au, C.; *ACS Sustainable Chem. Eng.* **2020**, *8*, 18034. [Crossref]

38. Kasperkiewicz, J.; Kovacich, J. A.; Lichtman, D.; *J. Electron Spectrosc.* **1983**, *32*, 123. [Crossref]
39. Cornaglia, L. M.; Lombardo, E. A.; *J. Phys-Condens. Mat.* **1993**, *5*, A225. [Crossref]
40. Wang, J.; Li, X.; Xia, Y.; Komarneni, S.; Chen, H.; Xu, J.; Xiang, L.; Xie, D.; *ACS Appl. Mater. Interfaces* **2016**, *8*, 8600. [Crossref]
41. Zheng, J. H.; Jiang, Q.; Lian, J. S.; *Appl. Surf. Sci.* **2011**, *257*, 5083. [Crossref]
42. Zhang, G.; Jin, X.; Zhang, Q.; Cheng, Y.; Chen, X.; Liu, Y.; Feng, X.; Yang, C.; *Catal. Sci. Technol.* **2020**, *10*, 4386. [Crossref]
43. Liu, J.; Xu, P.; Wang, P.; Xu, Z.; Feng, X.; Ji, W.; Au, C.; *Sci. Rep.* **2019**, *9*, 16988. [Crossref]
44. Babaei, Z.; Chermahini, A.; Dinari, M.; *J. Colloid Interf. Sci.* **2020**, *563*, 1. [Crossref]
45. Griffin, M.; Ferguson, G.; Ruddy, D.; Biddy, M.; Beckham, G.; Schaidle, J.; *ACS Catal.* **2016**, *6*, 2715. [Crossref]
46. Pilsl, M.; Engel, C.; *Nat. Commun.* **2020**, *11*, 1206. [Crossref]

Submitted: March 12, 2025
Published online: May 5, 2025